11-1-2018

Spatiotemporal filtering of high harmonics in solids

Christopher Q. Abadie
Louisiana State University

Mengxi Wu
Louisiana State University

Mette B. Gaarde
Louisiana State University

Recommended Citation

Abadie, C., Wu, M., & Gaarde, M. (2018). Spatiotemporal filtering of high harmonics in solids. *Optics Letters, 43* (21), 5339-5342. https://doi.org/10.1364/OL.43.005339

Letter Vol. 43, No. 21 / 1 November 2018 / Optics Letters 5339

Optics Letters

Spatiotemporal filtering of high harmonics in solids

Christopher Q. Abadie, Mengxi Wu, and Mette B. Gaarde*

Department of Physics and Astronomy, Louisiana State University, Baton Rouge, Louisiana 70803-4001, USA
**Corresponding author: gaarde@phys.lsu.edu*

Received 14 August 2018; revised 27 September 2018; accepted 28 September 2018; posted 1 October 2018 (Doc. ID 342362); published 24 October 2018

We study the macroscopic spatial and temporal properties of harmonic radiation generated by a model solid in the interaction with an intense, focused laser beam. We show that different temporal contributions to the harmonic yield can be separated in the spatial domain because they lead to radiation with different divergences, similar to what is observed in gas-phase harmonic generation. We show that applying a spatial filter in the far field results in a temporal separation of the two contributions upon refocusing, which yields spatially collimated harmonics, a spectrum with well-resolved peaks, and a subcycle time profile of the harmonic radiation with only one burst per half-cycle.

https://doi.org/10.1364/OL.43.005339

Since the first demonstration in 2011 [1], interest in high harmonic generation (HHG) in condensed media has been rapidly growing. HHG in solids has potential both as a bright, controllable source of ultrafast vacuum and extreme ultraviolet (VUV and XUV) light [2–6] and as a means of exploring ultrafast dynamics of electrons in the condensed phase [7–10]. For applications in harmonic spectroscopy and time-domain characterizations, in particular, it is important that the temporal coherence properties associated with the HHG process are well characterized so that they can be deconvoluted from measurements of target-specific dynamics [7,11,12].

The temporal coherence properties of solid-state HHG have been shown to depend strongly on the nonlinear generation mechanism [4,5,9,13], in which both intraband and interband processes contribute to the emission [2,5,7,9,14,15]. The HHG process can be described in momentum (k) space in terms of half-cycle-periodic electron dynamics on the band structure, initiated by tunnel ionization from the valence band (VB) to the conduction band (CB). The field-driven acceleration of the electron on the CB gives rise to an intraband current, whereas the time-dependent coherence between the population in the CB and VB gives rise to an interband polarization [2,14–16]. The cutoff energy in the harmonic spectrum is determined by the maximum bandgap [14,17], and excitation to higher lying CBs can give rise to secondary plateaus with higher cutoff energies [3,15]. The dynamics on the VB and CB are illustrated in the inset in Fig. 1(a), with the arrow connecting the two bands representing the interband polarization at a particular energy. The intraband harmonics will in general be emitted all at the same time each half-cycle, near the peaks of the electric field, whereas the interband harmonic radiation is emitted at different times and therefore exhibits an attochirp [5,9,15].

Harmonic spatial coherence has only been characterized in a few experiments [8,9], for which the harmonic radiation (in SiO_2) was dominated by the intraband contribution, leading to good spatial coherence. It is still an open question as to how the generation mechanism for and the propagation of the harmonic radiation in the macroscopic sample affects the spatiotemporal properties of the generated light. In a recent calculation incorporating propagation effects in one dimension, Floss and collaborators showed that well-resolved harmonic peaks could result from an initially unresolved spectrum [18]. This suggests that efforts to control the harmonic spatiotemporal coherence properties at the macroscopic level, which has been tremendously successful for HHG in gases [19–21], may also be applicable for HHG in solids.

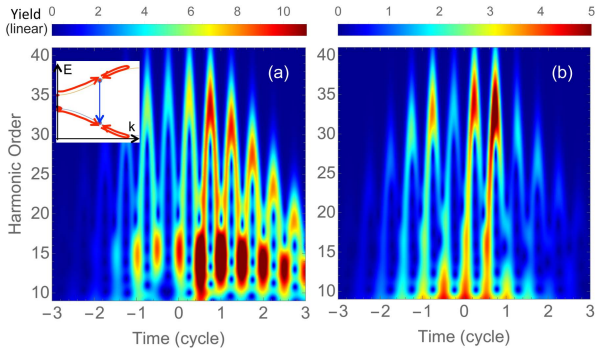

Fig. 1. Time-frequency profiles in the near field, (a) before and (b) after spatial filtering. Inset in (a) shows the laser-driven electron dynamics on the VB and CB during one-half laser cycle. Red arrows illustrate that each VB-CB energy difference (blue arrow) is entered twice: when the increasing (decreasing) vector potential accelerates (decelerates) the electron to that *k*-value.

In this Letter, we study the macroscopic spatial and temporal properties of the harmonic radiation generated by a model solid in the interaction with a intense, focused laser beam. We show that different temporal contributions to the harmonic yield can be separated in the *spatial* domain because they have different divergences, even in the absence of longitudinal phase matching. We also show that the harmonic divergence can be modeled analytically by considering the space- and time-dependent phase accumulated by an electron in a two-level system. The spatial separation means that applying a far-field spatial filter results in a temporal separation of the two contributions beyond the filter, which yields spatially collimated harmonics, a spectrum with well-resolved peaks, and a subcycle harmonic time profile with only one burst per half-cycle.

Our calculations proceed in three steps: first we calculate the microscopic nonlinear current generated by a one-dimensional periodic system interacting with an intense mid-infrared laser pulse, linearly polarized along the system axis. Then we calculate the macroscopic current density that would be produced across the focal plane of a focused laser beam interacting with a uniform distribution of identical periodic systems, mimicking one crystal plane. In the limit of an infinitely thin crystal, we approximate the total harmonic electric field at the exit of the crystal to be proportional to the macroscopic current density, and transform it to the far field. Finally, we apply a spatial filter in the far field and compare the (refocused) harmonic radiation to that of the original near-field distribution. We also show that the thin medium limit is a good approximation for the crystal response, given that the absorption lengths for above-bandgap light in many condensed media are on the order of a few to a few tens of nanometers (nm).

We calculate the nonlinear current by solving the time-dependent Schrödinger equation (TDSE) in the velocity gauge, using a basis of field-free Hamiltonian eigenstates (Bloch states) that form the band structure. For details, see [15,22]. In the velocity gauge, the harmonic spectrum can be calculated independently from each crystal momentum k as the Fourier transform of the time-dependent current $j_k(t) = -[\langle\psi_k(t)|\hat{p}|\psi_k(t)\rangle] + A(t)$ (in atomic units), and then added coherently. $A(t)$ is the laser vector potential, and the matrix elements of the momentum operator $\hat{p}$ are calculated from the Bloch states. Here, we include only the contribution from $k = 0$, which has the largest tunneling probability and therefore is expected to be dominant, at least at moderate intensities [14]. Furthermore, we have shown that the field-dressed states of the $k = 0$ multilevel system exactly reproduce the full band structure they originate from [22,23]. This means that the HHG process in the $k = 0$ system exactly mimics the electron dynamics on the band structure, in terms of tunneling (of an electron originating at the Gamma point), acceleration on the band (in the multilevel system, this is equivalent to the evolution of the dressed states with the vector potential), and coherence between the dressed states leading to emission. This approach has led to good agreement with experimental results in several cases [3,5,23].

We use a Mathieu-type periodic potential $V(x) = -0.37(1 + \cos(2\pi x/a_0))$ with lattice constant $a_0 = 8$ a.u. leading to a minimum (maximum) VB–CB bandgap of 4.2 eV (14.5 eV). We include the four lowest bands in the calculations, although only the VB and the lowest CB contribute significantly to the dynamics. The laser pulse vector potential has the form $A_0 f(t)\sin(\omega_1 t)$, where A_0 is the peak vector potential, ω_1 is the laser frequency, and the envelope $f(t) = \sin^2(\frac{\omega_1 t}{22})$ has a full width at half-maximum (FWHM) pulse duration of approximately four optical cycles. We use a central wavelength of 3.2 μm and a peak intensity of 0.87 TW/cm^2. This means that the primary plateau in the harmonic spectrum, which is dominated by the interband polarization [15], spans from harmonic 11 (H11) up to H37.

The cylindrically symmetric macroscopic electric field, $E(r, \omega)$, is calculated at the focus of a Gaussian laser beam with a waist of 20 μm, where r is the near-field radial coordinate and ω is the frequency. In an experiment, this would correspond to the crystal being positioned so that its back face is at the laser focus. We then calculate the far-field electric field at some distance L beyond the nonlinear medium, $E(r', \omega)$, within the paraxial approximation, as the Hankel transform of $E(r, \omega)e^{i\omega r^2/2Lc}$, where c is the speed of light. Finally, we also calculate the macroscopic harmonic signal that would be measured in a target area, after refocusing the harmonic radiation with a small mirror that also acts like a spatial filter. This is done by applying a trigonometric spatial filter with a FWHM (diameter) of 2 cm and then back transforming to the near field.

Figure 1(a) shows the harmonic time-frequency profile produced on axis in the laser focus ($r = 0$), calculated using a Gabor wavelet transform [24]. For all energies above the minimum bandgap, the time-frequency profile exhibits two bursts of light per half-cycle, corresponding to the two times the electron passes the k-space point on the conduction (and valence) band where the bandgap matches that energy. As the photon energy increases, the two times approach each other until there is only one emission time at the cutoff energy. This behavior is very similar to that found for HHG in gases, where each harmonic is emitted at least twice per half-cycle, corresponding to a so-called short or long quantum path followed by the continuum electron wave packet in real space [25]. For gas-phase harmonics, it is well known that the harmonic radiation associated with the two different paths separates in the far-field spatial domain, because of a different intensity-dependent phase imposed on the near-field radial profile [19]. It is thus natural to wonder whether a similar effect might occur in the macroscopic response from a condensed phase system.

Figure 2(a) shows the intensity profile of the harmonic radiation in the far field, $L = 1$ m beyond the laser focus. For improved visibility, we have smoothed the data using a $2\omega_1$ rolling average. The figure shows that the harmonic spatial profiles clearly have two contributions, one intense and narrow, extending to about 1 cm, and the other weaker and broader. As the photon energy increases toward the cutoff, the two contributions approach each other and eventually merge.

This behavior can be understood from the different radial phase imposed on the two different temporal contributions to the harmonic radiation (when, as in our case, it is dominated by the interband contribution). The phase accumulated by each contribution increases with emission time and is approximately proportional to the field strength (as we will show below), which varies across the laser focus. This means that the radial phase of the first (second) contribution is small (large), which leads to a small (large) divergence and a narrow (broad) peak in the far field. Likewise, since higher harmonics are emitted later (earlier) in the half-cycle for the first (second) contribution, they have larger (smaller) divergences than lower harmonics.

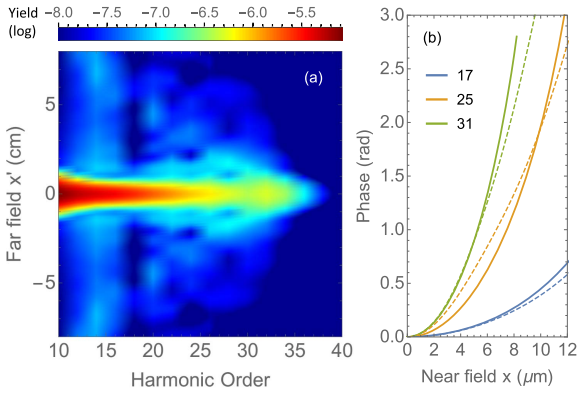

Fig. 2. (a) Far-field spatial-spectral profile, shown in log scale. (b) Near-field radial phase for H17, H25, and H31 (lowest to highest curves). Solid lines show two-level analytical prediction (see text); dashed lines show numerical result after far-field spatial filtering.

We can analytically calculate the laser-imposed radial phase variation of the harmonic radiation by approximating our periodic system as a two-level system. Then the instantaneous emission frequency corresponds to the instantaneous energy difference between the two levels in the field $E_i(t) = 2\sqrt{\Omega^2(t) + (\omega_{12}/2)^2}$. Here ω_{12} is the field-free energy difference (the bandgap in our system), $\Omega(t) = p_{12}A(t)$ is the Rabi frequency associated with the laser field, and p_{12} is the two-level transition matrix element. In each half-cycle, the electron tunnels from the lower to the upper level at $t = 0$ (at the zero of the vector potential) and the time-dependent dipole moment at emission time t_e has therefore accumulated a phase $\phi(t_e) = -\int_0^{t_e} E_i(t)\mathrm{d}t$. The field-dependent spectral phase accumulated at harmonic energy $\omega_\hbar$, due to the first contribution to that harmonic, therefore varies across the radial profile as

$$\phi_{\hbar 1}(r) = -\int_0^{t_1(r)} (E_i(r,t) - \omega_\hbar)\mathrm{d}t, \qquad (1)$$

where the emission time $t_1(r)$ (in the half-cycle at the peak of the pulse) is found from the earliest time where $E_i(r, t_1) = \omega_\hbar$, and the r-dependence comes from the variation of the peak vector potential across the laser focus.

Figure 2(b) (solid lines) shows the analytically calculated radial phase of the first contribution to three different harmonics. As expected from the discussion above, the radial phase variation is faster for the higher harmonics. The second contribution has much faster phase variations that become slower with increasing harmonic order (not shown). We note that in our analytical model, H31 is not generated beyond 8 μm when the laser intensity drops below its cutoff value. Figure 2(b) also shows the radial phase calculated numerically after applying the far-field spatial filter and back transforming to the near field (dashed lines). The small deviation between the two sets of curves results from both that (i) the spatial filter suppresses the second contribution but cannot eliminate it completely, and (ii) the two-level behavior is an approximation to the multilevel system used in the numerical calculations.

Finally, we consider the change in harmonic emission properties in the target area after spatial filtering. Figure 1(b) shows that the time-frequency profile has clearly changed to be largely dominated by the first emission peak. This is the most important result of our work—it means that a spatial filter can control the spectral and temporal coherence properties of the harmonic radiation from condensed phase materials.

We demonstrate the improved coherence properties of the filtered radiation further in Fig. 3, which compares the (a) radially integrated spectrum, and the (b, c) near-field radial profiles of H17 and H31 before and after the spatial filter. The unfiltered spectrum in Fig. 3(a) exhibits the characteristics of multiple interfering contributions that wash out the harmonic structure. In contrast, the spatially filtered spectrum shows well-resolved harmonic peaks through most of the plateau. Likewise, harmonic radial profiles are smooth and well behaved for the filtered radiation, in contrast to those of the unfiltered radiation. This indicates that also the spatial coherence properties have been significantly improved by the spatial filter. For the harmonics closest to the cutoff, the first and second contributions are not well separated in the spatial (or temporal) domain, and the filter is therefore less effective. We note that the total yield is clearly much lower in the filtered spectrum since the spatial filter blocks a substantial portion of the harmonic radiation. However, the yield in the harmonic peaks themselves is in general reduced by less than a factor of 10, indicating that the spatial filter mostly suppresses the more divergent, less coherent part of the harmonic emission.

We note that because of the very short absorption lengths of the harmonics in condensed phase materials, longitudinal phase matching plays no role in the quantum path selection demonstrated in Figs. 1(b) and 3. We have estimated the effect of propagation and absorption of the harmonics in the crystal by adding up the contribution from multiple crystal slices spanning a thickness of up to 300 nm. Each slice is multiplied by a frequency-dependent phase factor, due to the refractive index mismatch between the driving field and the harmonics (dispersion), as well as an amplitude factor due to absorption. We use optical constants of 1.9 and 1.6 for the refractive index of the fundamental and the harmonics, respectively, and 0.5 for

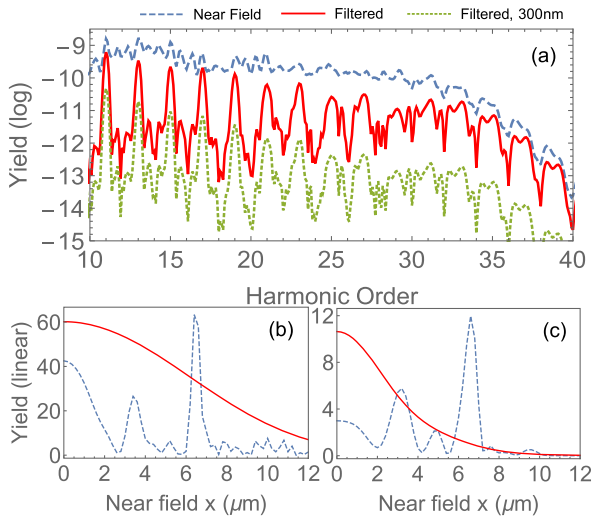

Fig. 3. (a) Radially integrated harmonic spectrum, and (b, c) near-field spatial profiles for (b) H17 and (c) H31. Dashed (solid) lines show near-field results before (after) spatial filtering in the far field. The filtered radial profiles for H17 (H31) have been scaled by 10 (5). Dotted line in (a) shows the filtered near field from a 300-nm-thick crystal (scaled for clarity).

the harmonic extinction coefficient. As an example, this means that the absorption length for radiation near H25 is about 20 nm. These values approximately mimic ZnO, which has a minimum bandgap of 3.3 eV [26,27], but are also generically representative of a range of transparent crystals. Figure 3(a) shows that the harmonic spectrum after (and before, not shown) spectral filtering is unchanged by the finite thickness, apart from a relative increase of the lower harmonics compared to the higher harmonics. We also find that beyond a thickness of ∼100 nm, the spectrum is essentially unchanged. Although these results are not surprising considering the high density of solids, it is nevertheless different from that of HHG in gases, where phase matching plays an important role in shaping harmonic coherence properties [28]. Note that to fully account for the crystal thickness, in particular the effect of the laser pulse propagation, would require solving the coupled wave equation and TDSE, which is beyond the scope of this work. However, recent calculations incorporating one-dimensional, longitudinal, propagation effects suggest that macroscopic effects of the laser field propagating through the crystal do influence the harmonic spectral resolution [18] and would thus be worthy of further consideration.

In summary, we have shown that multiple temporal contributions to the harmonic emission from a model solid separate spatially in the far field due to their different divergence properties, even in the absence of longitudinal phase matching. This means that a spatial filter placed in the far field results in a temporal separation of the two contributions upon refocusing, and thereby spatially collimated harmonics, a spectrum with well-resolved peaks, and a subcycle time profile of the harmonic emission with only one burst per half-cycle. Experiments have in general measured well-resolved harmonics even in the absence of spatial filtering [2,3,6,7,16], in contrast to the predictions of a variety of calculations [14,15,29–31]. Many calculations have employed short decoherence times to model electron–electron interactions, thereby suppressing processes similar to the second emission above [2,5,14,23]. Our results suggest that the macroscopic temporal and spatial, transverse, coherence properties of the harmonic radiation also play an important part in what will be measured in experiments, namely that it is primarily the promptly generated harmonic radiation (such as the first contribution discussed above) that will propagate in the forward direction, with limited divergence. It is also possible that the second contribution is very sensitive to imperfections and propagation-induced laser profile changes, making it even less collimated than discussed above and therefore less likely to be detected. This also suggests that looking at HHG from solids in reflection would yield different spatiotemporal properties of the harmonic light [32]. Another interesting prospect would be to consider the coherence properties of harmonics in the second plateau [3,5], which are emitted later than first-plateau harmonics since they result from population transferred to higher-lying CBs in a stepwise process, through the first CB. Our prediction based on the results above would then be that the coherence properties of these second-plateau harmonics would be more difficult to control through spatial filtering. Likewise, it would be interesting to study the spatiotemporal coherence properties of more realistic crystals such as those used in current experiments, for which the 3D band structure and density of states would be expected to play a role.

Funding. National Science Foundation (NSF) (PHY-1713671).

REFERENCES

1. S. Ghimire, A. D. DiChiara, E. Sistrunk, P. Agostini, L. F. DiMauro, and D. A. Reis, Nat. Phys. **7**, 138 (2011).
2. O. Schubert, M. Hohenleutner, F. Langer, B. Urbanek, C. Lange, U. Huttner, D. Golde, T. Meier, M. Kira, S. W. Koch, and R. Huber, Nat. Photonics **8**, 119 (2014).
3. G. Ndabashimiye, S. Ghimire, M. Wu, D. A. Browne, K. J. Schafer, M. B. Gaarde, and D. A. Reis, Nature **534**, 520 (2016).
4. F. Langer, M. Hohenleutner, U. Huttner, S. W. Koch, M. Kira, and R. Huber, Nat. Photonics **11**, 227 (2017).
5. Y. S. You, M. Wu, Y. Yin, A. Chew, X. Ren, S. Gholam-Mirzaei, D. A. Browne, M. Chini, Z. Chang, K. J. Schafer, M. B. Gaarde, and S. Ghimire, Opt. Lett. **42**, 1816 (2017).
6. Y. S. You, D. A. Reis, and S. Ghimire, Nat. Phys. **13**, 345 (2017).
7. G. Vampa, T. J. Hammond, N. Thiré, B. E. Schmidt, F. Légaré, C. R. McDonald, T. Brabec, and P. B. Corkum, Nature **522**, 462 (2015).
8. T. T. Luu, M. Garg, S. Y. Kruchinin, A. Moulet, M. T. Hassan, and E. Goulielmakis, Nature **521**, 498 (2015).
9. M. Garg, M. Zhan, T. T. Luu, H. Lakhotia, T. Klostermann, and A. G. E. J. Goulielmakis, Nature **538**, 359 (2016).
10. H. Liu, Y. Li, Y. S. You, S. Ghimire, T. F. Heinz, and D. A. Reis, Nat. Phys. **13**, 262 (2017).
11. A.-T. Le, R. R. Lucchese, S. Tonzani, T. Morishita, and C. D. Lin, Phys. Rev. A **80**, 013401 (2009).
12. S. B. Schoun, R. Chirla, J. Wheeler, C. Roedig, P. Agostini, L. F. DiMauro, K. J. Schafer, and M. B. Gaarde, Phys. Rev. Lett. **112**, 153001 (2014).
13. M. Hohenleutner, F. Langer, O. Schubert, M. Knorr, U. Huttner, S. W. Koch, M. Kira, and R. Huber, Nature **523**, 572 (2015).
14. G. Vampa, C. R. McDonald, G. Orlando, P. B. Corkum, and T. Brabec, Phys. Rev. B **91**, 064302 (2015).
15. M. Wu, S. Ghimire, D. A. Reis, K. J. Schafer, and M. B. Gaarde, Phys. Rev. A **91**, 043839 (2015).
16. S. Ghimire, A. D. DiChiara, E. Sistrunk, U. B. Szafruga, P. Agostini, L. F. DiMauro, and D. A. Reis, Phys. Rev. Lett. **107**, 167407 (2011).
17. M. Wu, S. Chen, S. Camp, K. J. Schafer, and M. B. Gaarde, J. Phys. B **49**, 062003 (2016).
18. I. Floss, C. Lemell, G. Wachter, V. Smejkal, S. A. Sato, X.-M. Tong, K. Yabana, and J. Burgdörfer, Phys. Rev. A **97**, 011401 (2018).
19. M. Bellini, C. Lyngå, A. Tozzi, M. Gaarde, T. Hänsch, A. L'Huillier, and C.-G. Wahlström, Phys. Rev. Lett. **81**, 297 (1998).
20. C. A. Haworth, L. E. Chipperfield, J. S. Robinson, P. L. Knight, J. P. Marangos, and J. W. G. Tisch, Nat. Phys. **3**, 52 (2007).
21. M. B. Gaarde, J. L. Tate, and K. J. Schafer, J. Phys. B **41**, 132001 (2008).
22. M. Wu, D. A. Browne, K. J. Schafer, and M. B. Gaarde, Phys. Rev. A **94**, 063403 (2016).
23. M. Wu, Y. You, S. Ghimire, D. A. Reis, D. A. Browne, K. J. Schafer, and M. B. Gaarde, Phys. Rev. A **96**, 063412 (2017).
24. Wolfram Research Inc., "Mathematica 11.0," 2016. See ContinuousWaveletTransform.
25. M. Lewenstein, P. Salières, and A. Lhuillier, Phys. Rev. A **52**, 4747 (1995).
26. H. Yoshikawa and S. Adachi, Jpn. J. Appl. Phys. **36**, 6237 (1997).
27. R. L. Hengehold, R. J. Almassy, and F. L. Pedrotti, Phys. Rev. B **1**, 4784 (1970).
28. C. M. Heyl, C. L. Arnold, A. Couairon, and A. L'Huillier, J. Phys. B **50**, 013001 (2017).
29. D. Golde, T. Meier, and S. W. Koch, Phys. Rev. B **77**, 075330 (2008).
30. N. Tancogne-Dejean, O. D. Mücke, F. X. Kärtner, and A. Rubio, Phys. Rev. Lett. **118**, 087403 (2017).
31. D. Bauer and K. K. Hansen, Phys. Rev. Lett. **120**, 177401 (2018).
32. G. Vampa, Y. S. You, H. Liu, S. Ghimire, and D. A. Reis, Opt. Express **26**, 12210 (2018).